Mineralium Deposita (2024) 59:699–716
https://doi.org/10.1007/s00126-023-01229-0

ARTICLE

Mapping hydrothermal alteration zones with short wavelength infrared (SWIR) spectra and magnetic susceptibility at the Pulang porphyry Cu-Au deposit, Yunnan, SW China

Cheng-Biao Leng[1] · Da-Zhao Wang[1] · Hai-Jun Yu[2] · Feng Tian[3] · Xing-Chun Zhang[4]

Received: 5 February 2023 / Accepted: 23 October 2023 / Published online: 8 November 2023

Abstract

Delineation of hydrothermal alteration zoning is important for exploration vectoring toward mineralization centers in porphyry systems, and shortwave infrared (SWIR) spectroscopy is widely used to map hydrothermal minerals distribution for porphyry Cu exploration. However, the SWIR method cannot effectively detect anhydrous alteration minerals (e.g., K-feldspar) in the potassic zone. Magnetite can be formed by potassic alteration and destroyed by phyllic (quartz-sericite-pyrite) alteration. The relative intensity of these two alteration types can be quantified by magnetic susceptibility. Here, we integrate the SWIR and magnetic susceptibility measurements to map hydrothermal alteration zones at the Pulang porphyry Cu-Au deposit in northwestern Yunnan, one of the largest porphyry deposits in the SW China-mainland SE Asia region. White mica, chlorite, and montmorillonite + kaolinite were identified in ~ 60%, ~ 30%, and ~ 15% of the analyzed samples from the Pulang deposit, respectively. Volumetric bulk magnetic susceptibility (K_{bulk}) values are high in the potassic-altered rocks, but low in phyllic-altered rocks. Using white mica as a proxy for sericite alteration, white mica-chlorite assemblage for chlorite-sericite alteration, chlorite-epidote-actinolite assemblage for propylitic alteration, montmorillonite-kaolinite-dickite assemblage for argillic alteration, and K_{bulk} ($> 0.5 \times 10^{-3}$ SI) for potassic alteration, we delineate the alteration zoning at Pulang. From the causative porphyry center outward, four alteration zones are delineated (potassic → chlorite-sericite → sericite → argillic). The ore-distal propylitic alteration was developed both in the shallow and deeper levels of the hydrothermal system, resembling typical porphyry-style alteration zoning patterns. Our work shows that high K_{bulk} value is a useful vector toward Cu mineralization at Pulang, whereas illite crystallinity (SWIR-IC), white mica Al–OH spectral absorption peak, and chlorite Fe-OH spectral absorption peak are less effective. We highlight that magnetic susceptibility measurement is an effective alteration-mapping method when mineralization is developed in the potassic zone (with largely aspectral minerals such as quartz, K-feldspar, and magnetite), while SWIR scalars are more useful when mineralization is developed in the phyllic and/or propylitic zones.

Keywords Alteration zoning · Shortwave infrared (SWIR) spectra · Magnetic susceptibility · Pulang porphyry Cu-Au deposit · Yidun terrane

Editorial handling: R. Wang

✉ Cheng-Biao Leng
lcb8207@163.com

✉ Da-Zhao Wang
dazhaowang@foxmail.com

[1] State Key Laboratory of Nuclear Resources and Environment, East China University of Technology, Nanchang 330013, China

[2] Yunnan Geological Survey, Kunming 650216, China

[3] Yejin Geological Team of Hubei Geological Bureau, Shiyan 442000, China

[4] State Key Laboratory of Ore Deposit Geochemistry, Institute of Geochemistry, Chinese Academy of Sciences, Guiyang 550081, China

Introduction

In porphyry Cu mineral systems, hydrothermal fluids exsolved from intermediate-felsic magmas would react with wallrocks and precipitate hydrothermal minerals (e.g., Richards 2003), forming predictable spatial distributions of hydrothermal alteration minerals, i.e., alteration zoning (e.g., Lowell and Guilbert 1970; Reed 1997; Seedorff et al. 2005; Sillitoe 2010; Cooke et al. 2014, 2017, 2020; Halley et al. 2015). Commonly, alteration zoning is featured by potassic alteration in the deep-level and central part, and transitions outward and/or upward through chlorite-sericite, sericitic, to (advanced-) argillic and propylitic alterations (e.g., Sillitoe 2010). Spatial changes in mineralization styles, metal ratios, and ore grades are commonly associated with specific hydrothermal alteration styles (e.g., Lowell and Guilbert 1970; Seedorff et al. 2005; Sillitoe 2010). Delineation of the alteration zones is thus critical for porphyry ore prospecting.

Hydrothermal alteration minerals in porphyry deposits are commonly fine grained and difficult to distinguish with confidence by visual examination. Lithogeochemical analyses, including whole-rock and mineral (EPMA and LA-ICP-MS) results, are useful to quantify hydrothermal alteration. However, these analyses are sample destructive and relatively costly (Ross et al. 2019). Shortwave infrared (SWIR) spectroscopy provides an inexpensive, non-destructive, and rapid way to identify hydrothermal alteration minerals (e.g., Thompson et al. 1999; Halley et al. 2015). This is based on the interactions between electromagnetic waves (1,300–2,500 nm wavelengths) and molecular bonds, and has been used to identify alteration minerals in various types of hydrothermal ore deposits, including volcanogenic massive sulfide (VMS) (e.g., Thompson et al. 2009; Laakso et al. 2016; Ross et al. 2019), epithermal (e.g., Yang et al. 2000, 2001; Chambefort et al. 2017; Wang et al. 2021), iron oxide-Cu-Au (e.g., Tappert et al. 2011, 2013), orogenic Au (Wang et al. 2017), and porphyry Cu deposits (e.g., Yang et al. 2005, 2012; Harraden et al. 2013; Guo et al. 2017). For instance, Chang et al. (2011) applied the SWIR method on the Lepanto high-sulfidation (HS) epithermal Cu-Au deposit, and found that the SWIR alunite absorption peak at ~ 1,480 nm shifts to higher wavelengths toward the ore-causative intrusion center. Harraden et al. (2013) found that high Cu-Au concentrations coincide with low AlOH absorption wavelength, and that SWIR is useful for distinguishing alteration types and distributions at the Pebble porphyry Cu deposit. Neal et al. (2018) argued that the wavelength positions and depths of absorption features at ~ 2,250 nm (Fe-OH absorption feature) and 2,340 nm (Mg-OH absorption feature) increase with distance from the orebody at the Batu Hijau porphyry Cu deposit, and that changes in absorption feature depth could represent a potential exploration vector.

The SWIR method can be used to identify infrared-active minerals to delineate phyllic, propylitic, and argillic alteration zones in porphyry Cu deposits. However, typical potassic alteration and ore minerals, including K-feldspar, secondary biotite, magnetite, anhydrite and sulfides, are either aspectral or they have spectra that can be affected by interference by other minerals (e.g., sericite, chlorite).

Previous studies have shown that potassic alteration is frequently accompanied by extensive magnetite crystallization (e.g., Lowell and Guilbert 1970; Lang et al. 2013), using the Fe^{2+} liberated from the alteration of hornblende (replaced by biotite) (Brimhall et al. 1985; Liang et al. 2009), whereas phyllic alteration tends to be magnetite destructive (e.g., Beane and Bodnar 1995; Seedorff et al. 2005; Purucker and Clark 2011; Riveros et al. 2014) as shown by the following reaction:

$$\begin{aligned} &Fe_3O_4(\text{magnetite}) + 6HS^- + 6H^+ + O_2 = 3FeS_2(\text{pyrite}) \\ &\quad + 6H_2O; Fe_3O_4(\text{magnetite}) + 6SO_4^{2-} + 12H^+ \\ &\quad = 3FeS_2(\text{pyrite}) + 6H_2O + 11O_2. \end{aligned}$$

As a result, the formation and destruction of magnetite would lead to changes in magnetic susceptibility, which can be used as a proxy to discern potassic versus phyllic alteration (Clark et al. 1992; Purucker and Clark 2011; Clark 2014). Potassic-altered rocks with high magnetic susceptibility have been reported in many porphyry copper deposits, e.g., at Chuquicamata and El Teniente (Chile), as high magnetic susceptibility is associated with the magnetite–biotite alteration (Astudillo et al. 2008, 2010). At Escondida, magnetic susceptibility is correlated positively with the degree of potassic- and chlorite alterations (Riveros et al. 2014). Hence, magnetic susceptibility measurement could complement SWIR analysis to better identify potassic alteration in porphyry deposits (Clark and Schmidt 2001; Astudillo et al. 2008, 2010; Shah et al. 2013).

In this study, we integrate the SWIR and magnetic susceptibility measurements to map hydrothermal alteration zones at the Pulang porphyry Cu-Au deposit, one of the largest porphyry deposits in China. Results may also help resolve controversies over the relationship between alteration style and Cu mineralization at Pulang: For example, Fan and Li (2006) and Li et al. (2011) suggested that the mineralization was mainly developed in the potassic zone, while Cao et al. (2019) argued that the mineralization was related to propylitic alteration.

Geologic background

The Pulang porphyry Cu-Au deposit is situated in the southern Yidun terrane, which is located between the Songpan–Garzê and Qiangtang terranes in the southeastern Tibetan Plateau (Fig. 1a) (Yin and Harrison 2000; Reid et al.

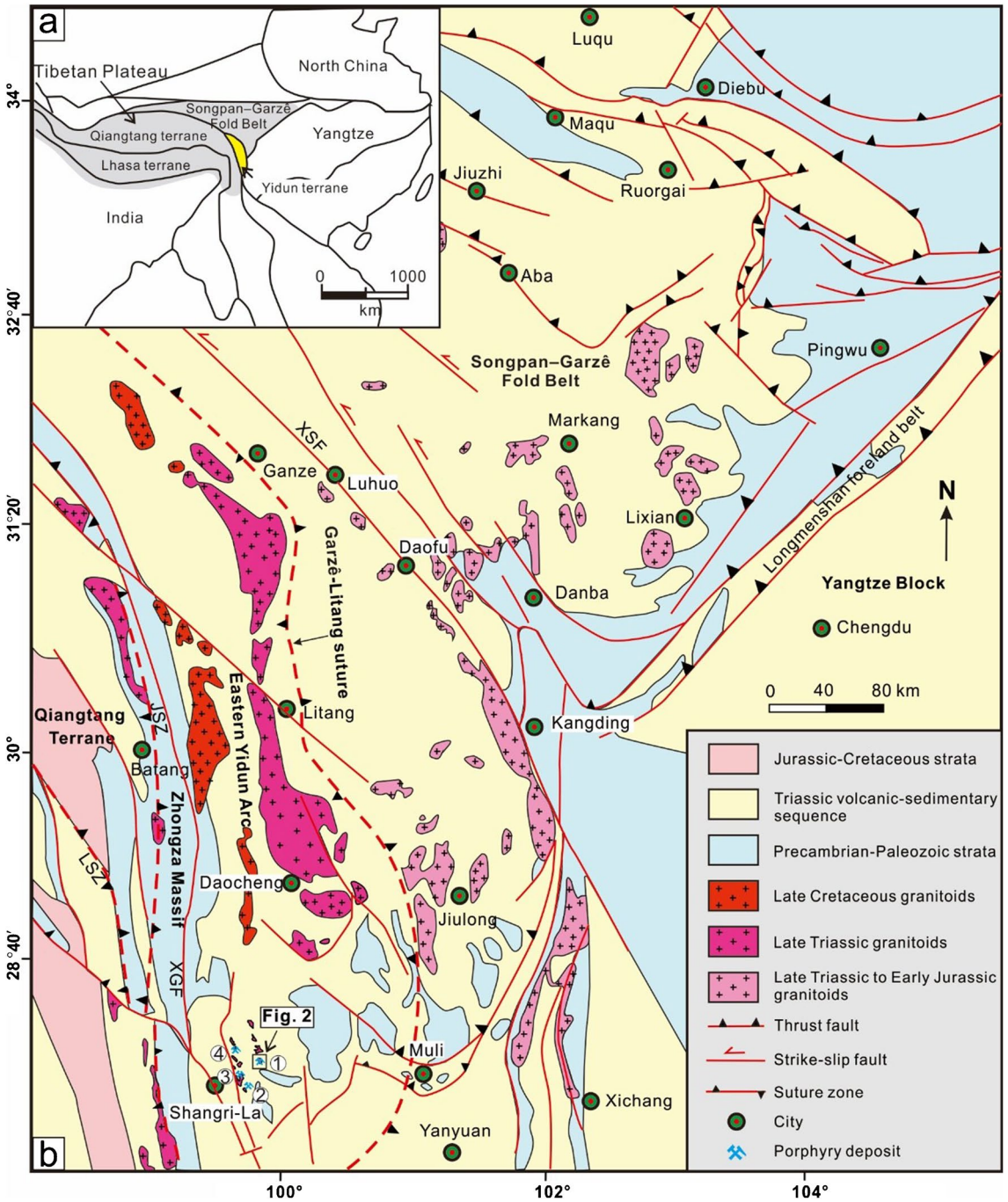

Fig. 1 (**a**) Tectonic framework of the Tibetan Plateau (modified after Leng et al. 2018a). (**b**) Geologic map of the Yidun terrane and its adjacent areas (modified after Tian et al. 2020). ①=Pulang deposit, ②=Chundu, ③=Xuejiping, ④=Lannitang. Abbreviations: GSZ=Garzê-Litang suture zone, JSZ=Jinsha suture zone, LSZ=Lancangjiang suture zone, XGF=Xiangchang–Geza fault, XSF=Xianshuihe fault

2005, 2007; Leng et al. 2012, 2014). The Yidun terrane is bounded by the Jinshajiang and Garzê–Litang sutures to the west and east, respectively (Hou and Mo 1991; Reid et al. 2007). It is commonly divided into the western Zhongza massif and the eastern Yidun arc by the NS-trending Xiangchang–Geza fault (XGF; Fig. 1b) (Reid et al. 2005; Leng et al. 2014). The Zhongza massif has similar lithological assemblages to the western margin of the Yangtze block, implying that it was part of the Yangtze block prior to the Early Permian (Chang 2000; Tian et al. 2020, 2022). The eastern Yidun arc was formed during the westward subduction of the Garzê-Litang Ocean in the Late Triassic (e.g.,

Leng et al. 2014). It is mostly overlain by the Triassic Yidun Group, consisting of slate and sandstone with minor limestone and flysch–volcanic interbeds and intrusive rocks (e.g., Hou et al. 2004). Many porphyry deposits were developed in the eastern Yidun arc, including the Pulang, Xuejiping, Chundu and Lannitang (Fig. 1b) (Li et al. 2011; Leng et al. 2012, 2014, 2018a, 2018b; Cao et al. 2019; Li et al. 2019; Guo et al. 2020).

The Pulang porphyry Cu-Au deposit contains proven reserves of ~ 4.31 million tonnes (Mt) Cu and 113 t Au, with an average grade of 0.34% and 0.09 g/t, respectively (Li et al. 2011; KPDI 2012). Pre-Quaternary strata in the ore district include mainly slate, sandstone, limestone and volcanic rocks of the Upper Triassic Tumugou Formation (Fig. 2). The ores are mostly hosted by the Pulang intrusive complex, which consists of five phases of porphyry stocks and dikes (Leng et al. 2018a, b; Fig. 2b – c). The stocks include pre-ore quartz diorite porphyry, syn-ore monzodiorite porphyry and quartz monzonite porphyry stocks, and post-ore granodiorite porphyry and andesite porphyry dikes (Leng et al. 2018a, b). Zircon U–Pb dates of the porphyries are 228–206 Ma (e.g., Wang et al. 2008; Leng et al. 2018a, 2018b; Cao et al. 2019; Li et al. 2019), whereas molybdenite from mineralized rocks yielded a Re-Os date of 216–213 Ma (e.g., Zeng et al. 2006; Cao et al. 2019).

Hydrothermal alteration at Pulang includes potassic, phyllic, propylitic and argillic alteration zones (e.g., Fan and Li 2006; Li et al. 2011; Cao et al. 2019; Chen et al. 2021; Zhao et al. 2021). Potassic alteration (the earliest alteration) developed hydrothermal K-feldspar, quartz, and minor biotite and trace magnetite in the form of veinlets, replacement of magmatic feldspar and hornblende (Fig. 3a), or vein halos (Fig. 3b). Phyllic (i.e., quartz + sericite ± pyrite) alteration overprinted the potassic and propylitic alterations, and occurred as pervasive replacement of feldspars and biotite or as vein halos (Fig. 3c–d). Chlorite-sericite alteration

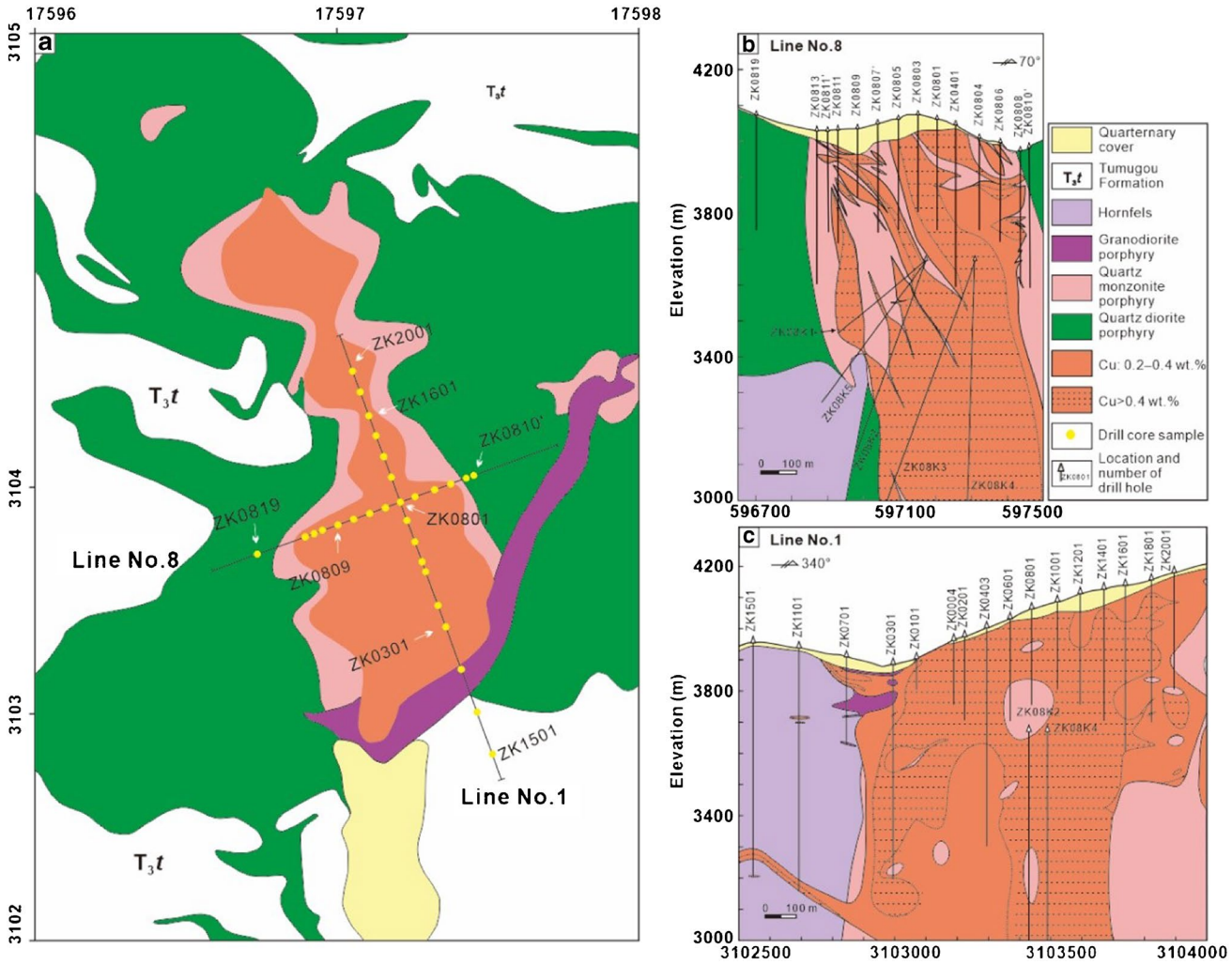

Fig. 2 Simplified (**a**) geological map (modified after Leng et al. 2018a, b) and profiles of (**b**) Line No. 8 and (**c**) Line No. 1 (modified after KPDI 2012) of the Pulang porphyry Cu-Au deposit

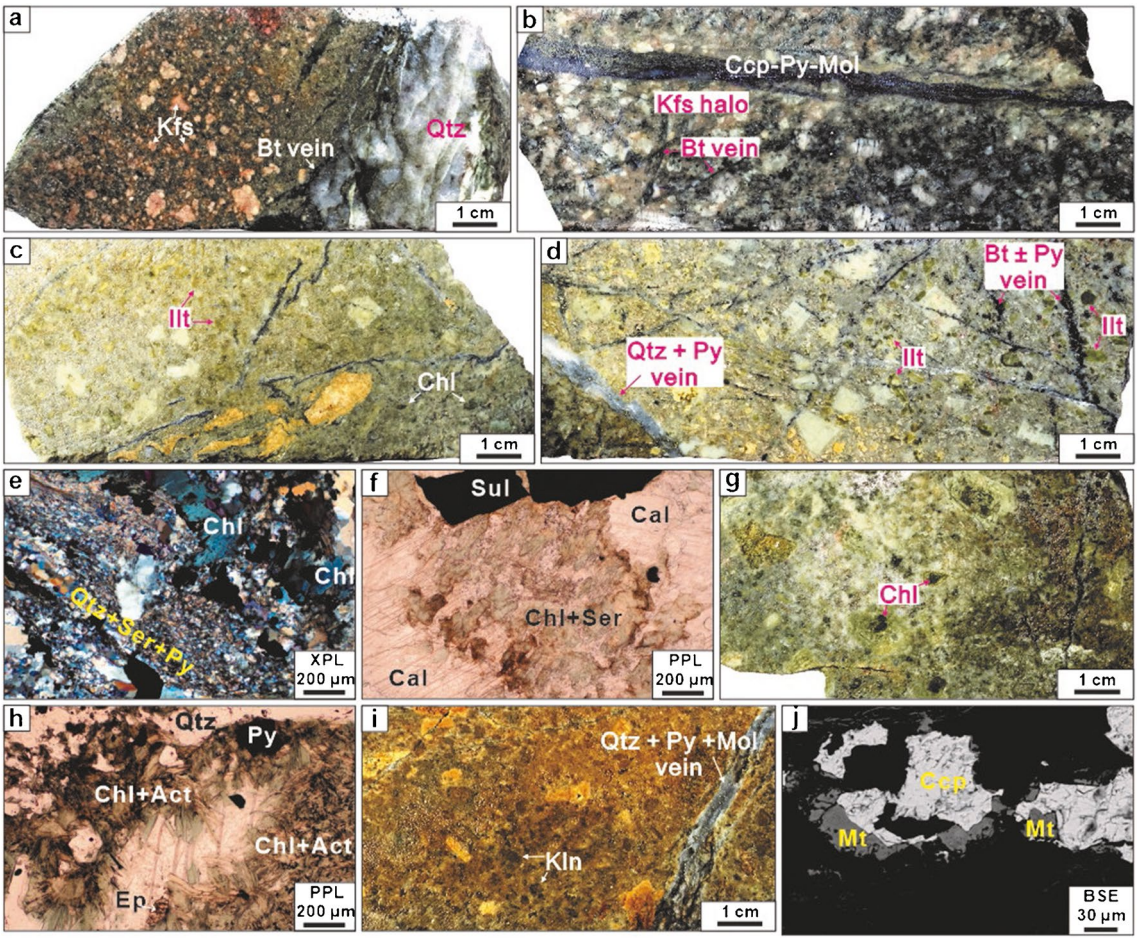

Fig. 3 Photographs of altered rock samples from Pulang porphyry Cu-Au deposit: (**a**) Potassic alteration, with magmatic feldspar replaced by hydrothermal K-feldspar; (**b**) Quartz ± chalcopyrite ± pyrite ± molybdenite vein with K-feldspar halos; (**c**) Sericite and chlorite alteration; (**d**) Sericite alteration, with magmatic feldspars and biotite replaced by illite; (**e**) Lineated quartz-sericite-pyrite assemblage overprinted on chlorite alteration in the quartz monzonite porphyry (XPL); (**f**) Chlorite-sericite-calcite-altered granodiorite porphyry (PPL); (**g**) Propylitic alteration, with magmatic hornblende and biotite replaced by chlorite and actinolite aggregates; (**h**) Propylitic-altered quartz monzonite porphyry with chlorite-actinolite-epidote assemblage (PPL); (**i**) Argillic alteration, with magmatic K-feldspars and plagioclase generally replaced by kaolinite and montmorillonite; (**j**) Magnetite-chalcopyrite assemblage in the potassic-altered quartz monzonite porphyry (BSE). BSE, backscattered electron; PPL, plane-polarized light; XPL, cross-polarized light. Mineral abbreviations: Act = actinolite, Bt = biotite, Cal = calcite, Ccp = chalcopyrite, Chl = chlorite, Ep = epidote, Ilt = illite, Kfs = K-feldspar, Mol = molybdenite, Mt = magnetite, Py = pyrite, Qtz = quartz, Ser = sericite, Sul = sulfide

contains muscovite, chlorite and epidote (Fig. 3e–f), and overprints preexisting potassic alteration assemblages. Propylitic alteration is characterized by extensive disseminations, veinlets or aggregates of chlorite, epidote, and actinolite (Fig. 3g–h). Argillic alteration is only developed locally in the central and shallow parts of the deposit. Igneous or hydrothermal feldspars were both replaced by clay minerals (kaolinite ± montmorillonite), causing the bleaching in the altered rocks (Fig. 3i).

As for the distribution of alteration zones and their spatial correlation to Cu mineralization at Pulang, Lian et al. (2005) identified phyllic, argillic and propylitic zones based on SWIR spectra, and pointed out that the ores were mainly developed between the potassic and phyllic zones. Fan and Li (2006) and Li et al. (2011) suggested that potassic and propylitic alteration was developed at the center and periphery of the deposit, respectively, and both alteration types were overprinted by late sericite and argillic alteration. Both studies show that mineralization was mainly developed in the potassic zone. In contrast, Cao et al. (2019) argued that the propylitic alteration is the most widespread alteration type that developed across the deposit and overprinted most of the potassic zone. Recently, Guo et al. (2021) delineated K-silicate, epidote-chlorite, chlorite-sericite, quartz-sericite, and argillic alteration zones, and found that the orebodies are mainly associated with the K-silicate and epidote-chlorite zones based on infrared spectroscopic analyses. Chen et al. (2021) and Zhao et al. (2021) identified a sericite alteration

zone at the eastern part of Pulang via ASTER (Advanced Spaceborne Thermal Emission and Reflection Radiometer) and WorldView-3 imaging, which may serve as proxies for targeting other mineralization centers. These different viewpoints on the alteration patterns at Pulang call for a more objective way to identify potassic alteration zones and their relation to the Cu-Au mineralization.

Sampling and analytical methods

SWIR spectral and magnetic susceptibility measurements were performed on 26 drill holes at Pulang. Locations of the drill holes and geological profiles of exploration Lines No. 1 and No. 8 are shown in Figs. 2 and 3. A total of 3,748 samples were collected mostly at 2-m intervals (see ESM Table 1), with the interval spacing locally up to 30 m. The samples of drill core are 5–10-cm long, and were rinsed and air-dried. Residual dust on the dry samples was removed with a soft brush prior to analysis. In our samples, the parts with veins/veinlets were avoided during analysis, as quartz-sulfide veins would greatly reduce the spectral signal and the accuracy of absorption depth-related scalars of SWIR (Wang et al. 2021) and cannot represent the altered rocks themselves.

SWIR spectral analysis

SWIR spectral data were collected from the 5–10-cm long drill core samples with a TerraSpec 4 spectrometer (Analytical Spectral Devices (ASD) Inc., Boulder, Colorado, USA), which measures spectral reflectance of 350 to 2,500 nm. Spectral resolution is 3 nm at a wavelength of 700 nm, 6 nm at 1,400 nm and 2,100 nm. The analytical acquisition window is a 2.5-cm-diameter circle. The "Dark Current" was set at 25, the "Spectrum Ave" was set to be 200 (measurement time of 20 s), and the "White Balance None Taken" was set at 400. The spectrometer was calibrated every 20 min, using a Spectralon white reference disk. Spectral files were created as scans at 2.5 cm-diameter circles on each sample and 200 scan acquisitions were set to yield an average spectrum for each measured spectrum (to improve the signal-to-noise ratio). Care was taken to analyze representative portions of the sample, and portions with high concentrations of quartz, K-feldspar or sulfides were avoided to minimize spectral interference. Detailed analytical procedures and instrumental parameters have been given by Chang and Yang (2012) and Ross et al (2019).

Spectral identification of minerals was processed with The Spectral Geologist (TSG) software version 8.0 (Spectral Geoscience Pty. Ltd.), which could automatically identify mineral types and calculate the proportions of minerals in each sample (Berman et al. 2017). The Spectral Assistant (TSA), a matching algorithm using the Mahalanobis distance (for pure minerals) and statistical techniques (for mineral mixtures), was applied to determine the log-linear mixture of no more than three minerals that best fit the sample spectrum (Ross et al. 2019). For mixed spectrum, the second or third minerals should have a weight of at least 15%, or the spectrum is interpreted as pure minerals. The scores of the standardized residual sum of squares (SRSS) are calculated to supervise the fitting result, with lower score signifying better fitting. If the final SRSS is over 500, the fit is considered poor and the TSA results are not reported (cf. Ross et al. 2019). The results are reported as aspectral if the spectrum is purely modeled as the background. The automatic TSG interpretation was checked manually via comparison with the standard spectral curves of the minerals measured, and the results with low signal-to-noise ratio and credibility are eliminated.

Magnetic susceptibility measurement

Volumetric bulk magnetic susceptibility (K_{bulk}) is defined by K = M/H, where M = induced magnetization of the material and H = inducing magnetic field (Rochette et al. 1992). All minerals are diamagnetic, but some minerals are strongly paramagnetic or ferromagnetic and swamp the diamagnetism. Paramagnetism is about 100 times stronger than diamagnetism, and paramagnetic minerals mainly include Fe-bearing silicates, including biotite, amphibole, pyroxene and Fe-rich clays. Ferromagnetic minerals have several orders of magnitude stronger susceptibilities than paramagnetic minerals, hence even very low content of ferromagnetic minerals could be detected. Ferromagnetic minerals, mainly comprise of Fe, Co and Ni, include magnetite, hematite, titanomagnetite and pyrrhotite.

The K_{bulk} values of our samples were measured at the same sites as the SWIR measurements, using a handheld SatisGeo KM-7 magnetic susceptibility meter (Czech Republic), with 10 kHz frequency and 10^{-6} SI sensitivity. For each analysis, the free space was measured before and after measuring the rock sample to determine the thermal drift of the oscillator. The muzzle of the magnetic susceptibility meter is 6 × 3 cm (rectangular), slightly larger than the TerraSpec 4 spectrometer. Each sample was measured thrice and the corresponding average was used to represent its K_{bulk} value.

Results

SWIR mineral identification

The infrared-active minerals have unique spectral wavelength compositions. White mica, including the muscovite solid-solution series from muscovite through phengite to

celadonite, is identified in the ~ 2,200 nm spectral wavelength (Al–OH absorption feature; Fig. 4a). The wavelength position tends to shift to longer wavelengths with the loss of Al in the white mica (Duke 1994). Montmorillonite has a distinct ~ 2,217 nm spectral absorption feature and lacks the ~ 2,350 nm O–H spectral absorption feature (Bishop et al. 2008), which is distinguishable from white micas. Kaolin group minerals have a narrow ~ 2,207 nm spectral absorption feature adjoined by a secondary 2,160 nm feature (Frost and Johansson 1998; Bishop et al. 2008), whilst carbonate has a 2,300 to 2,335 nm spectral absorption feature (Gaffey 1986). The intensity of the 2,160 nm absorption feature is influenced by the crystallinity of the respective kaolin group minerals (Frost and Johansson 1998), which can be used to identify the poorly- and well-crystalline kaolinite. Chlorite group minerals are characterized by ~ 2,250 nm and ~ 2,350 nm spectral absorption features (Fig. 4b), which shift to longer wavelengths with decreasing Mg/(Mg + Fe) ratio (King and Clark 1989; Bishop et al. 2008). Biotite has major absorptions at ~ 2,250 nm and ~ 2,330 nm, resembling those of chlorite. The two minerals can be differentiated with the ~ 2,400 nm absorption feature for Al-poor chlorite, which is much weaker than the equivalent ~ 2,390 nm absorption of biotite. Epidote has main absorption features at ~ 2,250 nm and ~ 2,340 nm, and the ~ 2,000 nm absorption feature is critical to distinguish chlorite from epidote (Lypaczewski and Rivard 2018).

The minerals identified with the TSG and optical microscopic and SEM observations at Pulang include mainly white mica, chlorite, epidote, montmorillonite, kaolinite, and biotite, with minor actinolite, dickite, gypsum, tourmaline, ankerite, hornblende, and dolomite (Fig. 5; ESM Table 1). Unreported and aspectral data were termed as NRA hereafter, which suggest that these samples are composed mainly of infrared inactive minerals or undergone other types of alteration.

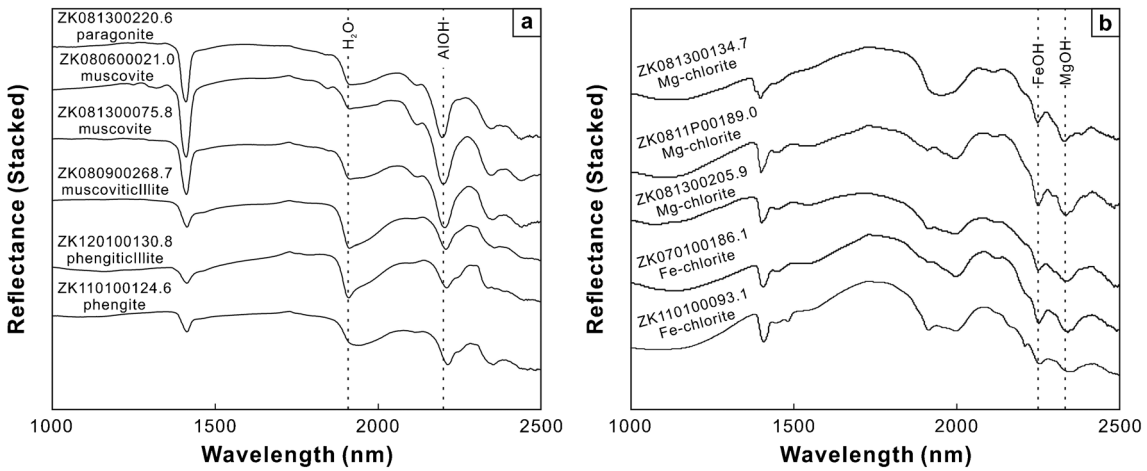

Fig. 4 Stacked spectra of white mica (**a**), and chlorite (**b**) from the Pulang porphyry Cu-Au deposit. The spectra are offset vertically to show variations in the depths of the 2,200 nm (a) and 2,250 nm (b) features

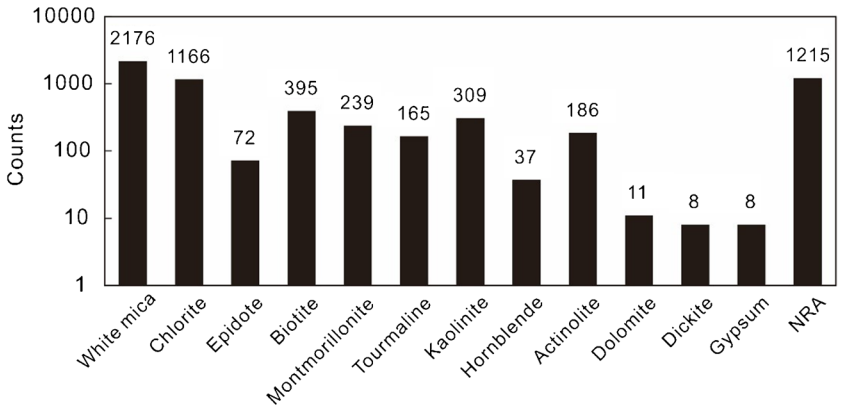

Fig. 5 Abundance of minerals and NRA (unreported and aspectral data) identified by TerraSpec at the Pulang porphyry Cu-Au deposit

White mica is the most pervasive mineral and is detected in 2,176 samples (58.1% of the total analyzed samples) (ESM Table 1). Chlorite and the montmorillonite ± kaolinite assemblage are detected in 31.1% and 14.6% of the analyzed samples, respectively. Other minerals, including actinolite, dickite, gypsum, tourmaline, and ankerite, are detected in less than 5% of the samples. 1,215 samples (32.4% of the total analyzed samples) are NRA.

Parameters of white mica and chlorite

The most frequently used SWIR parameters for white mica are the wavelength position of the Al–OH (~2,200 nm, wAlOH) absorption features and illite crystallinity (SWIR-IC) (Chang et al. 2011; Tian et al. 2019). The wAlOH can be used to approximate the white mica composition, which tends to shift to longer wavelength with lower octahedral Al (Al^{vi}) content (Duke 1994; Jones et al. 2005; Yang et al. 2011). At Pulang, the wAlOH values tend to increase in the order of paragonite → muscovite → illite → phengite (Fig. 4a). The wAlOH values of mica are affected by kaolinite and dickite, and analyses with these minerals are excluded to calculate the wAlOH values. The wAlOH values of the analyzed samples range from 2,188 to 2,224 nm, indicating a wide range of white mica compositions (Fig. 4a).

SWIR-IC is calculated using a depth ratio of the ~2,200 nm absorption divided by that of the ~1,900 nm absorption (e.g., Chang et al. 2011; Tian et al. 2019). The SWIR-IC values are primary controlled by temperatures (Frey 1987), with the illite crystallinity increasing with temperature (Chang et al. 2011; Yang et al. 2012). The SWIR-IC values can be interfered by minerals with a ~1,900 nm absorption feature, including montmorillonite, chlorite, epidote, carbonate and kaolinite (Wang et al. 2021), and analyses containing these minerals are excluded to get accurate SWIR-IC values. A total of 774 samples are filtered out to calculate the SWIR-IC values, which range from 0.2 to 6.9, and the highest ones are found in hornfels (ESM Table 1).

The SWIR parameters for chlorite are the wavelength position of the Fe-OH (~2,250 nm, wFeOH) and Mg-OH (~2,350 nm, wMgOH) absorption features (Fig. 4b). Because the chlorite wMgOH commonly coincides with the secondary mica AlOH and carbonate MgOH absorption features at ~2,350 nm, only the chlorite wFeOH is used in this study (Herrmann et al. 2001; Ross et al. 2019). The chlorite wFeOH values are controlled by temperature, pH and composition of chlorites (Herrmann et al. 2001; Han et al. 2018; Neal et al. 2018), and the wFeOH tends to shift to longer wavelength with decreasing Mg / (Mg + Fe) ratio (King and Clark 1989; Bishop et al. 2008). At Pulang, the wFeOH values of Fe-chlorite are higher than those of Mg-chlorite (Fig. 4b). The chlorite wFeOH values are affected by dark micas and epidote that share the same ~2,250 nm absorption feature (Ross et al. 2019), and therefore, we only show wFeOH values for samples without dark micas and epidote. The wFeOH values of the Pulang samples range from 2,240 nm to 2,257 nm. Herrmann et al. (2001) found that white micas could cause anomalously low wFeOH values of chlorites. Ross et al. (2019) suggested a correction for the wFeOH values based on the proportion of white mica in the sample. Here, we use the correction method of Ross et al. (2019) to correct the wFeOH values of chlorites; the corrected wFeOH values range from 2,241 nm to 2,264 nm (ESM Table 1).

Magnetic susceptibility

The K_{bulk} values represent the sum of all the ferromagnetic, paramagnetic, and diamagnetic mineral phases present in the rocks (Riveros et al. 2014). The K_{bulk} values of the Pulang samples vary from 0.007×10^{-3} to 25.810×10^{-3} SI (see ESM Table 1), displaying a wide range. Different altered rocks show distinctive K_{bulk} ranges. In general, the average K_{bulk} values of the altered-rock samples are 0.160×10^{-3} SI (sericite alteration, $n = 120$), 0.292×10^{-3} SI (propylitic alteration, $n = 155$), 0.130×10^{-3} SI (argillic alteration, $n = 86$), and 0.535×10^{-3} SI (potassic alteration, $n = 450$). The highest K_{bulk} values are found in the potassic-altered rocks and ores, that were mostly identified as NRA by SWIR (Fig. 6). This indicates that magnetite is the main magnetic mineral. Slightly lower K_{bulk} values are measured in the chlorite-altered rocks, whilst the lowest K_{bulk} values are measured in the sericite-altered rocks. Such trend of K_{bulk} variation among potassic-, chlorite-, and sericite-altered rocks is consistent with that identified by Clark (2014).

The relationships between K_{bulk} values and Cu grades vary in different drill holes. In ZK0801, high K_{bulk} values are commonly associated with high Cu grade, while low K_{bulk} values are corresponding to barren rocks but with high contents of white mica and chlorite (Fig. 6a). In ZK08K2, most samples are from potassic-altered rocks with high K_{bulk} values, and the correlation between K_{bulk} value and Cu grade are weak (Fig. 6b). Based optical microscopic and SEM observations, we found that the main magnetic minerals in the potassic rocks and ores are magnetite and pyrrhotite, respectively.

Mapping of mineral and magnetic susceptibility distribution

Mineral contents estimated by SWIR data are inherently relative, i.e., it only serves to give the proportion of spectral minerals. We visualized the relative contents of white mica, chlorite, and montmorillonite + kaolinite and magnetic susceptibility values of core samples in drilling holes along the No. 8 and No. 1 exploration lines in Figs. 7 and 8, respectively.

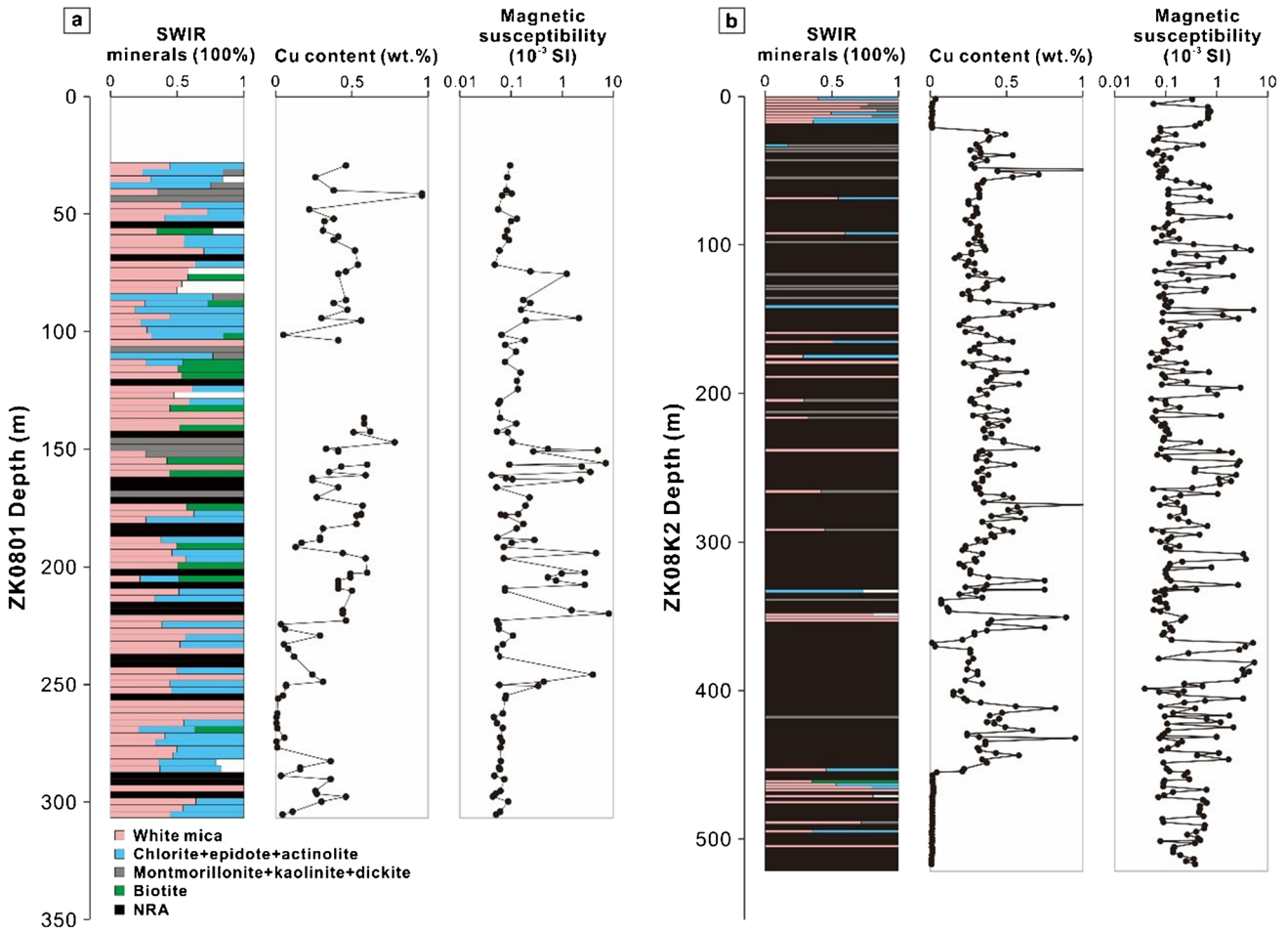

Fig. 6 Strip logs of (**a**) ZK0801 and (**b**) ZK08K2 drillholes from the Pulang porphyry Cu-Au deposit, showing relative mineral abundance, Cu contents (%) and magnetic susceptibilities (K_{bulk} values, 10^{-3} SI). Data are listed in ESM Tables 1 and 2

In the profile of Line No. 8 (Fig. 7), white mica is widely distributed around (but not in) the orebodies (indicated by Cu ≥ 0.2%). At shallow levels (< 300-m depth), the chlorite is distributed distally from the ores (Fig. 7b), whilst white mica alteration was developed between the orebodies and chlorite alteration zone. The montmorillonite + kaolinite assemblage is mostly distributed in the deposit central (shallow level), showing no significant spatial relationship with the Cu mineralization (Fig. 7c). The NRA samples are mainly distributed at deep levels (> 300 m-depth), mostly in the interspace between white mica zones (Fig. 7d). The NRA zone overlaps nicely with the orebodies, indicating that the NRA samples comprise mainly sulfides, consistent with the SEM results (Fig. 3j). The high K_{bulk} values of core samples in drill holes along the Line No. 8 are distributed at shallow levels in the eastern part of the deposit (but in deep levels elsewhere), with a clear increasing trend of their values toward the ores (Fig. 7e–f). The high-grade ores (Cu > 0.4%) have higher magnetic susceptibility than the country rocks, with the highest K_{bulk} value obtained from a sample from the orebody margin. Samples of relatively low K_{bulk} values are mainly located in the white mica-rich zones.

Similar to the Line No. 8, white mica is widely distributed in drill-core samples from the Line No. 1 (Fig. 8a). Chlorite is mainly distributed in the ore-proximal wallrocks (Fig. 8b), whilst the montmorillonite + kaolinite assemblage is distributed in shallow levels of the deposit (Fig. 8c). The high K_{bulk} values of the Line No. 1 are widespread in the central part (Fig. 8f), spatially associated with the distribution of high-grade orebodies (Cu > 0.4%; Fig. 8e).

Discussion

SWIR and magnetic signatures and their relationships to alteration zones

In porphyry Cu deposits, the key minerals for potassic (biotite and K-feldspar), phyllic (quartz and sericite), propylitic (chlorite, epidote, albite and carbonate), and argillic

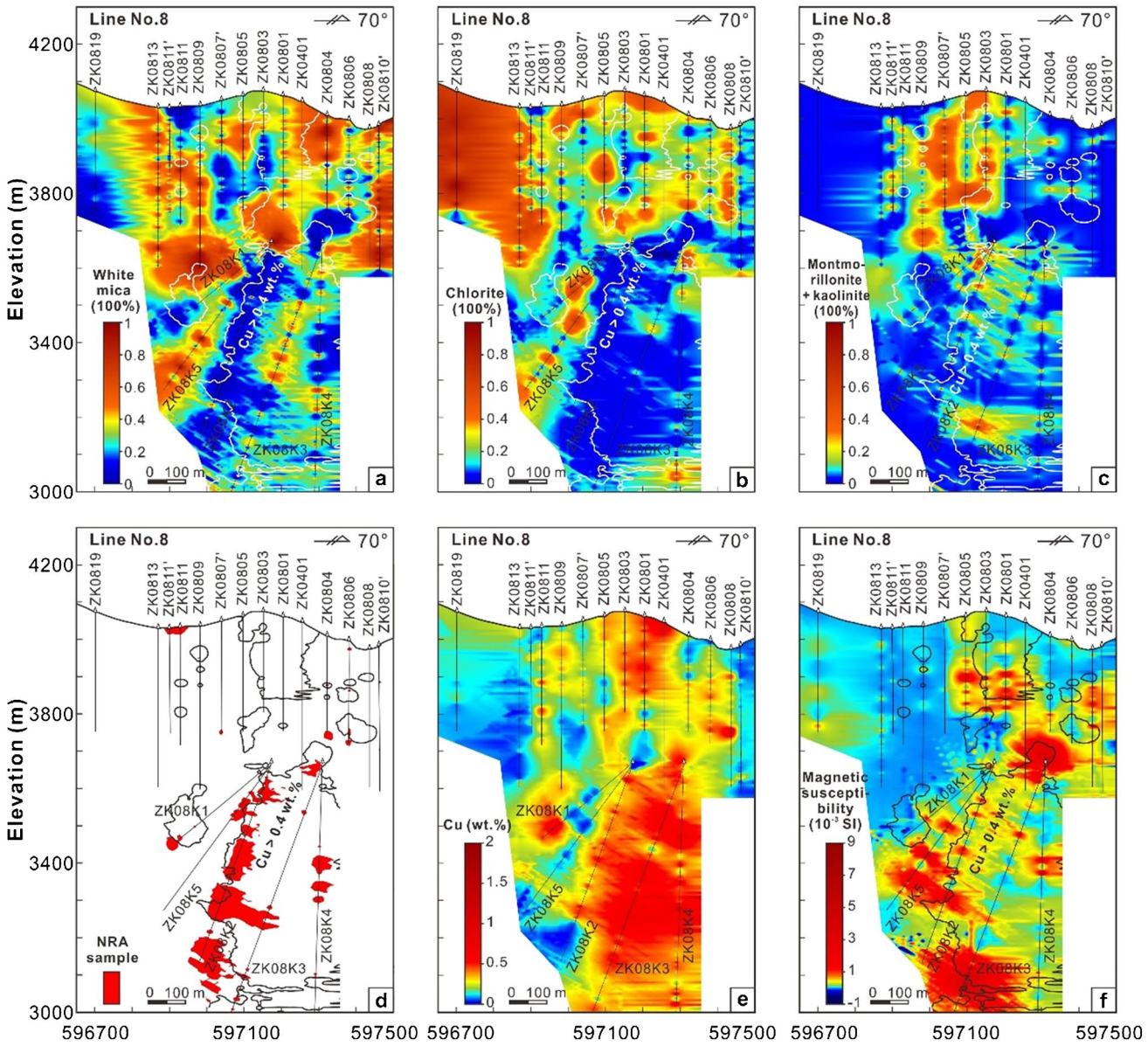

Fig. 7 Profiles (with minimum curvature grid) of (**a**) white mica, (**b**) chlorite, (**c**) montmorillonite + kaolinite, (**d**) NRA, (**e**) Cu contents, and (**f**) K_{bulk} values for Line No. 8 at Pulang porphyry Cu-Au deposit. Alteration mineral contents based on SWIR analyses. Data are listed in ESM Tables 1 and 2

(montmorillonite, dickite, kaolinite and pyrophyllite) alteration zones are distinct (e.g., Sillitoe 2010). Based on field and microscopic observations and the SWIR-identified minerals, we use white mica as a proxy for sericitic alteration, chlorite + epidote ± actinolite for propylitic alteration, and montmorillonite + kaolinite ± dickite for argillic alteration at Pulang. Other minerals (e.g., gypsum, tourmaline and ankerite), which are only present in a small number of samples (Fig. 5), are not discussed here. Owing to the fact that the TSG gives no more than three minerals for each sample, the dominant alteration style is defined by the mineral assemblage that accounts for over 30% of that particular sample. As shown in ESM Figures A1 and A2, many alteration zones overlap with each other, especially the sericitic and propylitic zones, which could represent overlapping chlorite-sericite alteration (cf. Sillitoe 2010).

Potassic alteration could be better identified by integrating the SWIR spectra with magnetic susceptibility measurements. During the potassic alteration stage, hydrothermal magnetite can be formed by incorporating the Fe^{2+} liberated when biotite replaced hornblende (Brimhall et al. 1985) or from the hydrothermal fluids (Rusk et al. 2004). The subsequent sericitic alteration would alter some magmatic/hydrothermal magnetite to pyrite (Sillitoe 2010; Purucker

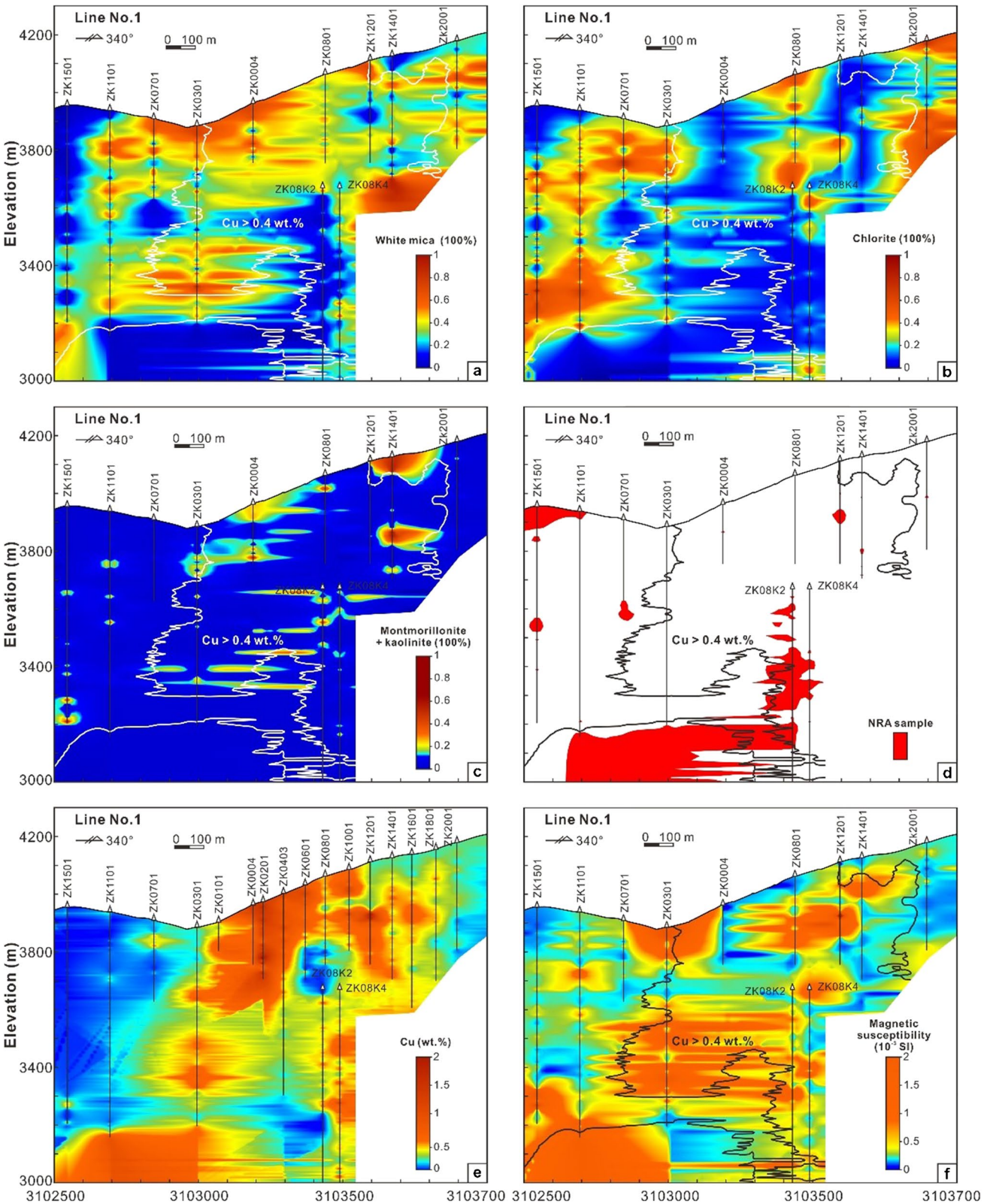

Fig. 8 Profiles (with minimum curvature grid) of (**a**) white mica, (**b**) chlorite, (**c**) montmorillonite + kaolinite, (**d**) NRA, (**e**) Cu contents, and (**f**) K_{bulk} values for Line No. 1 at Pulang porphyry Cu-Au deposit. Alteration mineral contents based on SWIR analyses. Data are listed in ESM Tables 1 and 2

and Clark 2011; Riveros et al. 2014). Thus, magnetite formation and destruction could form distinctive features for the potassic and sericitic alteration, respectively. A very small concentration of magnetite could render compelling magnetic signals, and thus relatively high magnetic susceptibility values of samples could indicate potassic alteration. Such correlations have been observed in many world-class porphyry Cu deposits. For example, different alteration zones at Escondida have distinctive and narrow-range K_{bulk} values, with those of the potassic zone ($> 5 \times 10^{-3}$ SI) being up to two orders of magnitude higher than those of the sericitic zone ($< 5 \times 10^{-4}$ SI) (Riveros et al. 2014).

There are some precautions for using the magnetic susceptibility to identify potassic alteration, because ore-barren magmatic rocks (many with magmatic magnetite) can also have higher and lower K_{bulk} values than sericite- and potassic-altered rocks, respectively (Astudillo et al. 2010; Riveros et al. 2014). For example, ore-barren magmatic rocks at the El Teniente deposit have K_{bulk} values ($< 10^{-4}$ SI) lower than that of the pervasive potassic-altered and mineralized rocks (Astudillo et al. 2010). In general, mafic rocks (esp. unaltered/weakly-altered ones) have higher K_{bulk} values than felsic ones (Astudillo et al. 2010; Kodama and Hinnov 2014). Therefore, the magnetic susceptibility comparison should be done within individual lithological units.

The potassic-altered rocks from the Pulang deposit have higher K_{bulk} values (average values $= 0.535 \times 10^{-3}$ SI) than other types of altered rocks. Therefore, we suggest a minimum K_{bulk} threshold of 0.5×10^{-3} SI to delineate the potassic zone at Pulang (Fig. 9).

From the deposit center outward and from the bottom upward, the alteration zones comprise potassic, chlorite-sericite, phyllic and argillic ones, with distal propylitic alteration occurred in all levels (Fig. 9). This resembles the common porphyry-style alteration zoning pattern (Lowell and Guilbert 1970; Sillitoe 2010) and the previously field-mapped Pulang alteration zoning based on geological and mineralogical characteristics (Li et al. 2011; Cao et al. 2019). Our results suggest a strong spatial relationship among alteration styles, SWIR mineral identification, and intensities of magnetic susceptibility at Pulang (Figs. 7 and 8), and reveal the potential of integration of the magnetic susceptibility and SWIR measurements to effectively delineate various alteration zones (incl. potassic) in porphyry Cu deposits.

Implications for exploration of porphyry deposits

Integration of the magnetic susceptibility and SWIR data serves as a useful exploration vector. The high K_{bulk} value coincides spatially with the orebodies (Figs. 7 and 8), and the K_{bulk} values are roughly correlated with Cu contents ($R^2 = 0.47$ for the average Cu content and average K_{bulk} value; Fig. 10a). Specifically, the K_{bulk} values show variations as the Cu contents increases, changing from scattered values when Cu < 0.1%, to increased ones for Cu = 0.1–0.7%, and then to decreased values when Cu > 0.7%. This can be explained

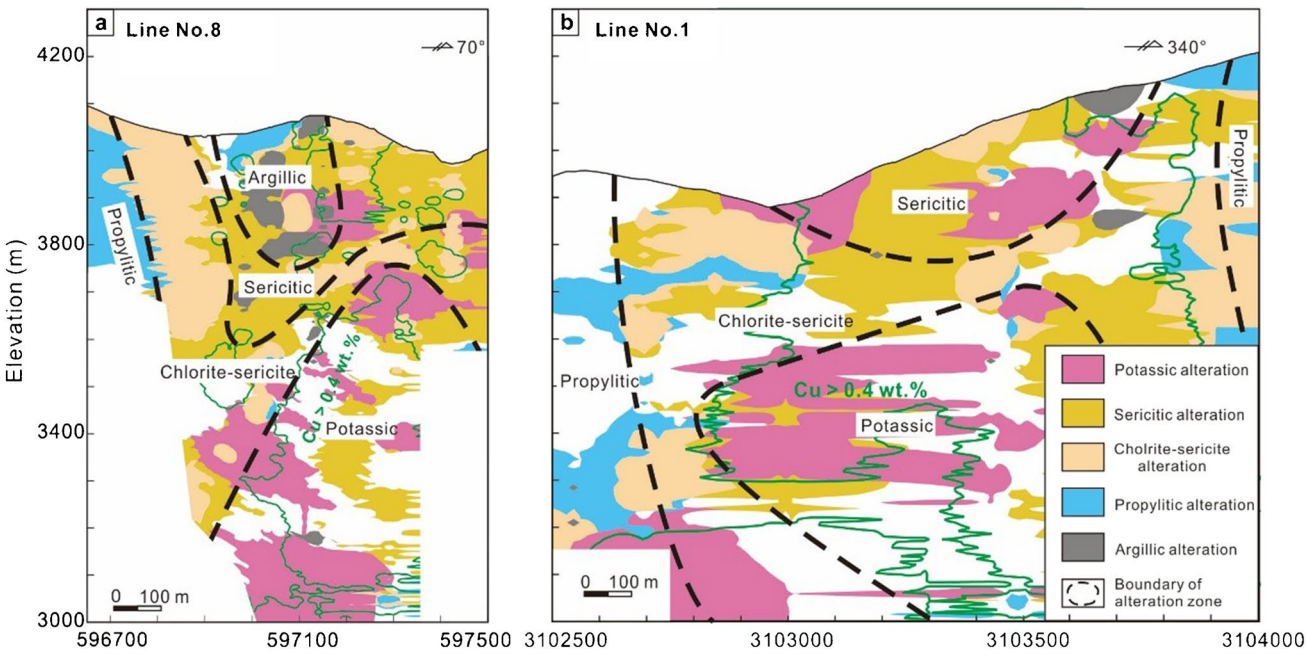

Fig. 9 Alteration profiles of Line No. 8 (**a**) and Line No. 1 (**b**) at Pulang porphyry Cu-Au deposit based on SWIR and magnetic susceptibility data

by the fact that the relatively low-Cu samples (Cu < 0.1%) are mainly phyllic-/propylitic-altered or unaltered with variable K_{bulk} values. Samples with moderate Cu values (Cu = 0.1–0.7%) are primarily potassic-altered with high magnetite and pyrrhotite contents, and thus their K_{bulk} value is relatively high. The high-Cu (Cu > 0.7%) samples contain chalcopyrite, bornite and pyrite. Their ferromagnetic mineral contents, and thus their K_{bulk} values, are relatively low.

Many studies have shown that the wAlOH, SWIR-IC and wFeOH values can vector toward the mineralization center (Yang et al. 2011; Tappert et al. 2013; Halley et al. 2015). At Pulang, the Cu mineralization is broadly associated spatially with white micas with low wAlOH values (Figs. 11a and 12a). Such spatial association is more distinct along Line No. 8 (Fig. 11a) than Line No. 1 (Fig. 12a), except for the shallow level along Line No. 1 (which shows low wAlOH in the high-Cu area). However, there is no correlation between Cu contents and wAlOH values ($R^2 = 0.01$, Fig. 10b). Although samples with low wAlOH values commonly have high Cu contents, not all the Cu-rich samples have low wAlOH values (Fig. 10b).

High SWIR-IC values of white micas spatially coincide with Cu mineralization, but in general the SWIR-IC values of white micas do not show any distinct trend toward the orebodies (Figs. 11b and 12b), and there is no correlation between the SWIR-IC values and Cu contents (Fig. 10c). Generally, it is suggested that SWIR-IC is a good paleo-thermal indicator in hydrothermal systems, with high SWIR-IC values corresponding to higher paleotemperatures (Frey 1987; Wang et al. 2021). At Pulang, high-SWIR-IC samples are distal to the mineralized monzonite porphyry, which if the above assumption is true, would suggest that the ore-distal fluids were of higher temperature than ore-proximal fluids, which is unlikely. Thus, the SWIR-IC value from Pulang is not a good indicator of the fluid migration path.

The relationships between Cu grades and wFeOH values at Pulang are complex. In the Line No. 1 profile (Fig. 12c), a decreasing wFeOH trend is observed from ZK1501 (~ 400 m south of the main ore zone) to ZK0701 in the main ore zone, whereas such trend is not distinct in the Line No. 8 profile (Fig. 11c). The wFeOH values show no correlation with Cu content (Fig. 10d), and samples with high Cu content (> 1%) commonly have no wFeOH values of chlorite, indicating high grade ores contain minor chlorite.

Overall, the SWIR-IC, wAlOH and wFeOH values are not robust mineralization indicators at Pulang, although low wAlOH values correlate locally to the mineralized zones. The usefulness of these values also varies in

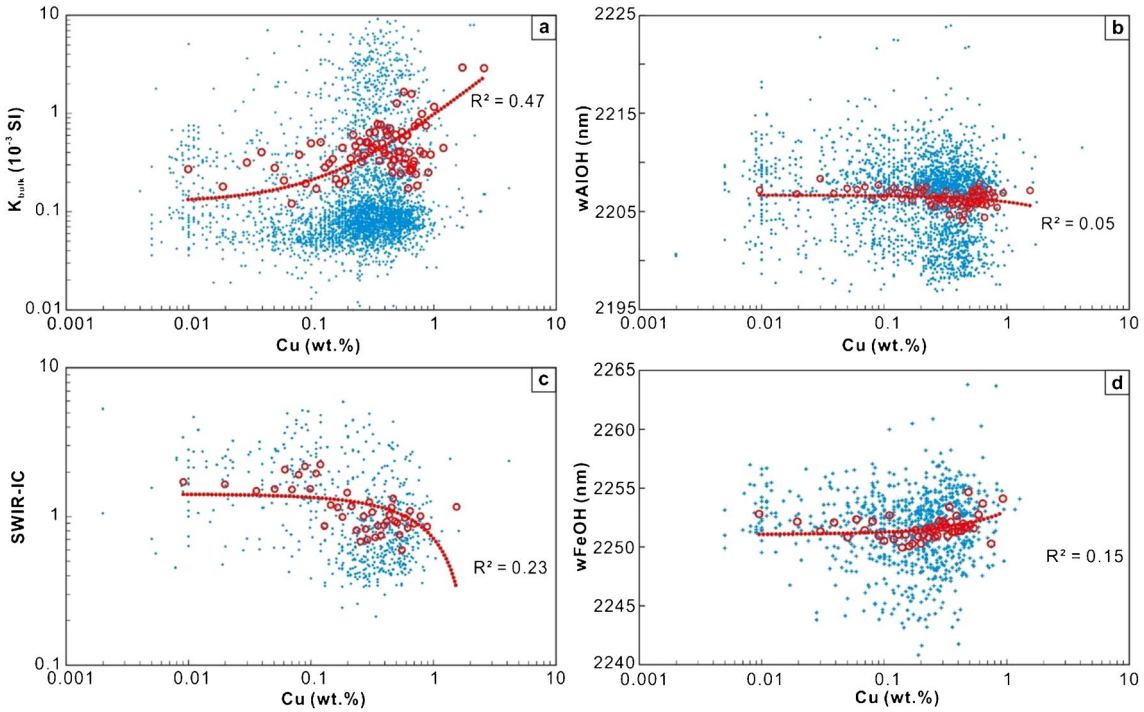

Fig. 10 Plots of Cu content vs. (**a**) K_{bulk}, (**b**) wAlOH, (**c**) SWIR-IC, and (**d**) wFeOH values for the core samples from the Pulang porphyry Cu-Au deposit. Blue cross and red circle denote the original and calculated average values, respectively. The average value is calculated using the following rules: The dataset is firstly grouped by Cu content, and then the average values of K_{bulk}, wAlOH, SWIR-IC and wFeOH values are calculated for each group. For groups with > 10 data points, the averages Cu content and the aforementioned parameters are calculated in those groups. For groups with < 10 data points, the average is calculated based on the adjacent 10 samples

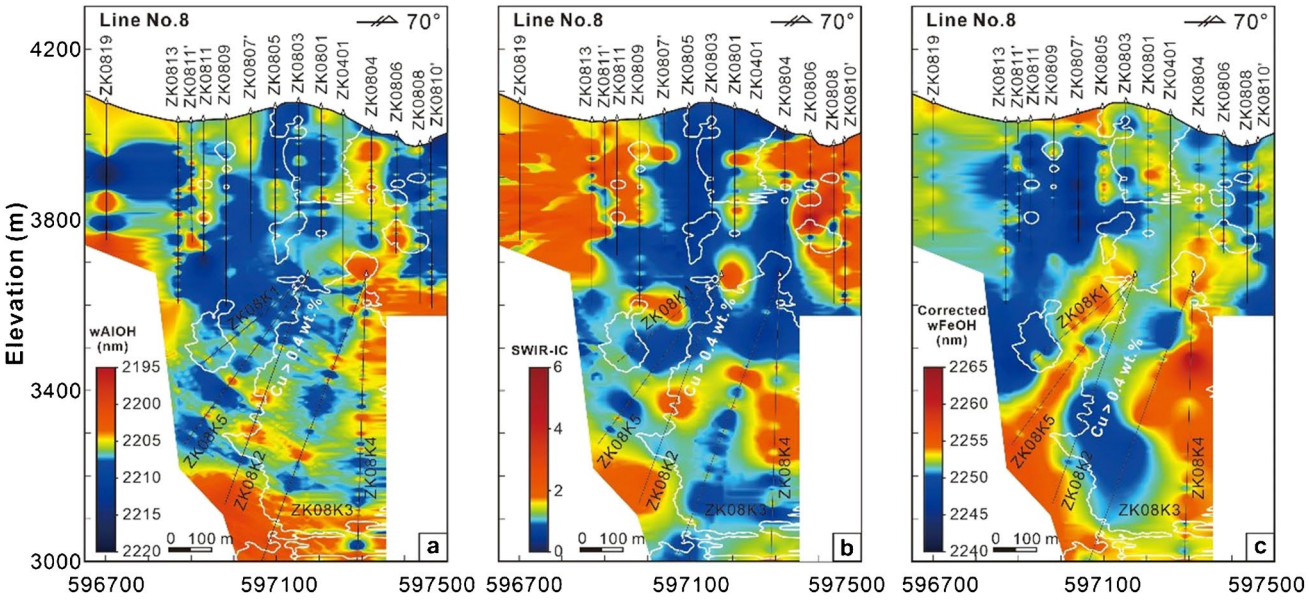

Fig. 11 Profiles (with minimum curvature grid) of (**a**) wAlOH values, (**b**) SWIR-IC values, and (**c**) corrected wFeOH values for Line No. 8 at Pulang porphyry Cu-Au deposit. Data are listed in ESM Table 1

different porphyry Cu deposits. For example, at Niancun, Yang et al. (2012) showed that the ore-proximal white micas have higher SWIR-IC (> 1.6) and lower wAlOH values (< 2,203 nm) than their ore-distal counterparts. At Jiama, Guo et al. (2017) showed that ore-related altered rocks have relatively high wAlOH values, and the wAlOH value (> 2,206 nm) increases with Cu-Mo grade. Neal et al. (2018) found that the chlorite wFeOH values of propylitic altered samples increase with distance from the orebody at Batu Hijau, whereas Han et al. (2018) argued that the chlorite from closer to the orebodies have higher wFeOH values.

The different usefulness of wAlOH and wFeOH values as vectors to ore zones may be caused by:

(1) The wAlOH, SWIR-IC and wFeOH values can be influenced by formation temperatures (Frey 1987; Yang et al. 2012), fluid compositions and pH values (Halley et al. 2015; Tian et al. 2019), rock permeabilities (Wang et al. 2021), and the physiochemical properties of the white micas and chlorites (Jones et al. 2005; Wang et al. 2021). Although many methods have been developed to preclude the interferences of mineral mixing (Lypaczewski and Rivard 2018; Ross et al. 2019; Wang et al. 2021), the influence of rock permeabilities and types could not be filtered out.

(2) Ores in porphyry Cu deposits are developed in different alteration zones (Sillitoe 2010), affecting the SWIR data interpretation. For example, the SWIR-IC values can be affected by interference from minerals with ~ 1,900 nm absorption features (e.g., montmorillonite, chlorite, epidote, carbonate and kaolinite) (Thompson et al. 2009), the wFeOH values are affected by the existence of dark and white micas (Herrmann et al. 2001; Ross et al. 2019), and aspectral minerals (e.g., quartz, feldspar, and sulfides) could flatten the spectral patterns and affect the SWIR-IC and wFeOH calculation (Wang et al. 2021). If the ores are associated primarily with potassic alteration, the wAlOH and SWIR-IC values of white micas would be significantly influenced by the aspectral minerals, causing poor spatial correlation between the SWIR values and ores, such as that in the case of Pulang. If the ores are associated with phyllic alteration, the wAlOH and SWIR-IC values could be indicative of mineralization, as is the case of the Gangjiang porphyry (Tian et al. 2019) and Jiama (Guo et al. 2017) porphyry-skarn deposits. The wFeOH value would be more useful if the ores are located in the propylitic zone (Herrmann et al. 2001; Jones et al. 2005).

(3) The SWIR values (SWIR-IC, wAlOH and wFeOH) are statistical methods, and the quality and reliability of the data would depend on the number of samples (Doublier et al. 2010). Therefore, the observed trends in SWIR-IC, wAlOH and wFeOH may just represent local phenomenon: For example, the Pulang Line No. 1 is represented by a lower sample density than Line No. 8. The wFeOH value decreases toward the ore zone in Line No. 1, but this trend is not observed in Line No. 8. Therefore, the wFeOH is not a robust exploration vector, and its reliability may be influenced by the sample density.

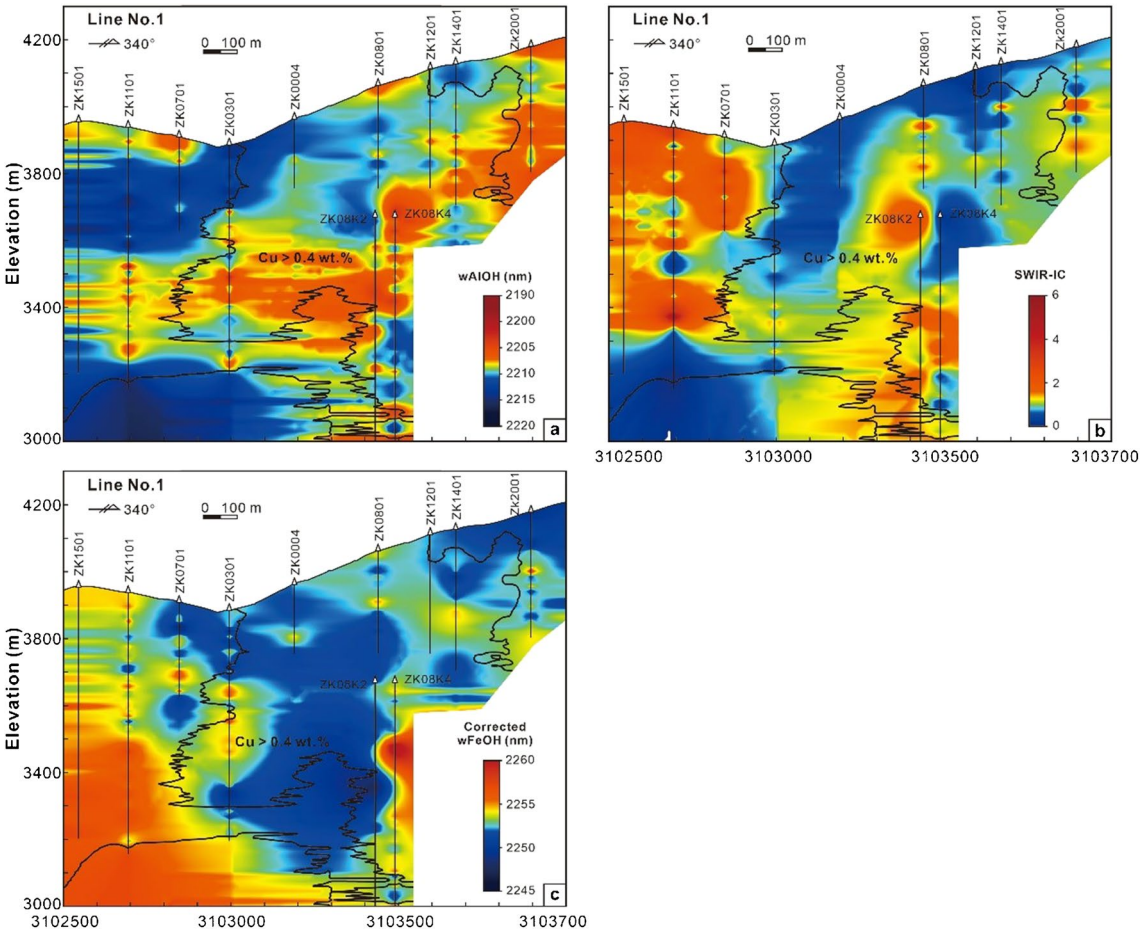

Fig. 12 Profiles (with minimum curvature grid) of (**a**) wAlOH values, (**b**) SWIR-IC values, and (**c**) corrected wFeOH values for Line No. 1 at Pulang porphyry Cu-Au deposit. Data are listed in ESM Table 1

Conclusions

The integration of SWIR and magnetic susceptibility (K_{bulk}) measurements from drill core samples from the Pulang porphyry Cu-Au deposit can effectively delineate the various alteration zones, including the spatial distribution of potassic, phyllic, propylitic and argillic alteration zones. This study further confirms that ores at Pulang were mainly formed within the potassic alteration zone, while mineralization also occurred in the chlorite-sericite and phyllic alteration zones, particularly in the central and upper part of the deposit. In contrast, mineralization was infrequent within the distal propylitic alteration zones.

The best exploration vector at Pulang is the high K_{bulk} values, which are highest in the ore-proximal potassic zone, while the SWIR-IC, wAlOH, and wFeOH values have limited exploration implications at Pulang. SWIR scalars of white mica and chlorite can indicate the mineralization zone when it is mainly hosted by phyllic or propylitic alteration, respectively, whereas magnetic susceptibility is a more effective vectoring tool when the mineralization is developed in the potassic zone.

Supplementary Information The online version contains supplementary material available at https://doi.org/10.1007/s00126-023-01229-0.

Acknowledgements We appreciate Xilian Chen, Kaixuan Li, Taoliang Chen, Jinwei Mao, and Feng Liang for assistance during the field investigations. We also appreciate the Yunnan Diqing Nonferrous Metals Co. Ltd. for funding this project. Kai Yang is thanked for the insightful discussion during the analyses of SWIR data. Suggestions by two anonymous reviewers, associate editor Rui Wang and editor Karen Kelley greatly improved the manuscript.

Funding This study was financially supported by the National Natural Science Foundation of China (NSFC) (42022021, 92062101, and 42173026), the Second Tibetan Plateau Scientific Expedition and Research project (2021QZKK0301).

Declarations

Competing interests The authors declare no competing interests.

References

Astudillo N, Roperch P, Townley B, Arriagada C, Maksaev V (2008) Importance of small-block rotations in damage zones along transcurrent faults. Evidence from the Chuquicamata open pit. Northern Chile Tectonophysics 450:1–20

Astudillo N, Roperch P, Townley B, Arriagada C, Chauvin A (2010) Magnetic polarity zonation within the El Teniente copper–molybdenum porphyry deposit, central Chile. Miner Deposita 45:23–41

Beane RE, Bodnar RJ (1995) Hydrothermal fluids and hydrothermal alteration in porphyry copper deposits, In: Pierce FW, Bohm JG (eds.) Porphyry copper deposits of the American Cordillera, 20: Tucson, Arizona Geological Society Digest 83–93

Berman M, Bischof L, Lagerstrom R, Gu Y, Huntington J, Mason P, Green A (2017) A comparison between three sparse unmixing algorithms using a large library of shortwave infrared mineral spectra. IEEE Trans Geosci Remote Sens 1–23

Bishop JL, Lane MD, Dyar MD, Brown AJ (2008) Reflectance and emission spectroscopy study of four groups of phyllosilicates: smectites, kaolinite-serpentines, chlorites and micas. Clay Miner 43:35–54

Brimhall GH, Agee C, Stoffregen R (1985) The hydrothermal conversion of hornblende to biotite. Can Mineral 23:369–379

Cao K, Yang ZM, Mavrogenes J, White NC, Xu JF, Li Y, Li WK (2019) Geology and genesis of the giant Pulang porphyry Cu-Au district, Yunnan, southwest China. Econ Geol 114:275–301

Chambefort I, Lewis B, Simpson MP, Bignall G, Rae AJ, Ganefianto N (2017) Ngatamariki geothermal system: Magmatic to epithermal transition in the Taupo Volcanic Zone, New Zealand. Econ Geol 112:319–346

Chang EZ (2000) Geology and tectonics of the Songpan-Ganzi Fold Belt, southwestern China. Int Geol Rev 42:813–831

Chang ZS, Yang ZM (2012) Evaluation of inter-instrument variations among short wavelength infrared (SWIR) devices. Econ Geol 107:1479–1488

Chang ZS, Hedenquist JW, White NC, Cooke DR, Roach M, Deyell CL, Garcia J, Gemmell JB, McKnight S, Cuison AL (2011) Exploration tools for linked porphyry and epithermal deposits: Example from the Mankayan intrusion-centered Cu-Au district, Luzon, Philippines. Econ Geol 106:1365–1398

Chen Q, Zhao ZF, Zhou JX, Zeng M, Xia JS, Sun T, Zhao X (2021) New insights into the Pulang porphyry copper deposit in Southwest China: Indication of alteration minerals detected using ASTER and WorldView-3 data. Remote Sensing 13:2798

Clark DA (2014) Magnetic effects of hydrothermal alteration in porphyry copper and iron-oxide copper–gold systems: A review. Tectonophysics 624–625:46–65

Clark DA, Schmidt PW (2001) Petrophysical properties of the Goonumbla volcanic complex, NSW: Implications for magnetic and gravity signatures of porphyry Cu-Au mineralisation. ASEG Extended Abstracts 2001:1–4

Clark DA, French DH, Lackie MA, Schmidt PW (1992) Magnetic petrology: Application of integrated rock magnetic and petrological techniques to geological interpretation of magnetic surveys. Explor Geophys 23:65–68

Cooke DR, Hollings P, Wilkinson JJ, Tosdal RM (2014) Geochemistry of porphyry deposits. In: Holland HD, Turekian KK (eds) Treatise on geochemistry, 2nd edn. Elsevier, Oxford, pp 357–381

Cooke DR, Agnew P, Hollings P, Baker M, Chang Z, Wilkinson JJ, Ahmed A, White NC, Zhang L, Thompson J, Gemmell JB, Danyushevsky L, Chen H (2020) Recent advances in the application of mineral chemistry to exploration for porphyry copper–gold–molybdenum deposits: detecting the geochemical fingerprints and footprints of hypogene mineralization and alteration. Geochem: Explor Environ Anal 20:176–188

Cooke DR, Agnew P, Hollings P, Baker M, Chang ZS, Wilkinson JJ, White NC, Zhang LJ, Thomas J, Gemmell JB, Fox N, Chen HY, Wilkinson CC (2017) Porphyry indicator minerals (PIMS) and porphyry vectoring and fertility tools (PVFTS) – Indicators of Mineralization Styles and Recorders of Hypogene Geochemical Dispersion Halos, Proceedings of Exploration 17. Sixth Decennial International Conference on Mineral Exploration: 457–470

Doublier MP, Roache T, Potel S (2010) Short-wavelength infrared spectroscopy: A new petrological tool in low-grade to very low-grade pelites. Geology 38:1031–1034

Duke EF (1994) Near infrared spectra of muscovite, Tschermak substitution, and metamorphic reaction progress: Implications for remote sensing. Geology 22:621–624

Fan YH, Li WC (2006) Geological characteristics of the Pulang porphyry copper deposit, Yunnan: Geology in China 33: 352–362 (in Chinese with English abs.)

Frey M (1987) Very low-grade metamorphism of clastic sedimentary rocks, In: Frey M (ed.) Low Temperature Metamorphism: Glasgow, Blackie and Son 9–58

Frost RL, Johansson U (1998) Combination bands in the infrared spectroscopy of Kaolins—A drift spectroscopic study. Clays Clay Miner 46:466–477

Gaffey SJ (1986) Spectral reflectance of carbonate minerals in the visible and near infrared (0.35-2.55 microns); calcite, aragonite, and dolomite. Am Miner 71:151–162

Guo N, Tomas C, Tang JX, Tong QX (2017) Mapping white mica alteration associated with the Jiama porphyry-skarn Cu deposit, Central Tibet using field SWIR spectrometry. Ore Geol Rev 108:147–157

Guo JH, Leng CB, Zhang XC, Zafar T, Chen WT, Zhang W, Tian ZD, Tian F, Lai CK (2020) Textural and chemical variations of magnetite from porphyry Cu-Au and Cu skarn deposits in the Zhongdian region, northwestern Yunnan SW, China. Ore Geol Rev 116:103245

Guo DX, Liu X, Zhang HL, Zhang ZG (2021) The infrared spectroscopy characteristics of alteration and mineralizationin the porphyry copper deposit in Pulang, Yunnan Province. Rock Miner Anal 40: 698–709 (in Chinese with English abs.)

Halley S, Dilles JH, Tosdal RM (2015) Footprints: hydrothermal alteration and geochemical dispersion around porphyry copper deposits. Soc Econ Geol Newsl 100:12–17

Han J, Chu G, Chen H, Hollings P, Sun S, Chen M (2018) Hydrothermal alteration and short wavelength infrared (SWIR) characteristics of the Tongshankou porphyry-skarn Cu-Mo deposit, Yangtze craton, Eastern China. Ore Geol Rev 101:143–164

Harraden CL, McNulty BA, Gregory MJ, Lang JR (2013) Shortwave infrared spectral analysis of hydrothermal alteration associated with the Pebble porphyry copper-gold-molybdenum deposit, Iliamna, Alaska. Econ Geol 108:483–494

Herrmann W, Blake M, Doyle M, Huston D, Kamprad J, Merry N, Pontual S (2001) Short wavelength infrared (SWIR) spectral analysis of hydrothermal alteration zones associated with base metal sulfide deposits at Rosebery and western Tharsis, Tasmania, and Highway-Reward, Queensland. Econ Geol 96:939–955

Hou ZQ, Gao YF, Qu XM, Rui ZY, Mo XX (2004) Origin of adakitic intrusives generated during mid-Miocene east–west extension in southern Tibet. Earth Planet Sci Lett 220:139–155

Hou ZQ, Mo XX (1991) A tectono-magmatic evolution of Yidun island arc in Sanjiang region. Contribution to the Geology of the Qunghai-Xizang (Tibet) Plateau 21:153–165 (in Chinese with English abs.)

Jones S, Herrmann W, Gemmell JB (2005) Short wavelength infrared spectral characteristics of the HW Horizon: Implications for exploration in the Myra Falls volcanic-hosted massive sulfide camp, Vancouver Island, British Columbia, Canada. Econ Geol 100:273–294

King TVV, Clark RN (1989) Spectral characteristics of chlorites and Mg-serpentines using high-resolution reflectance spectroscopy. J Geophys Res: Solid Earth 94:13997–14008

Kodama KP, Hinnov LA (2014) Rock magnetism, In: Kodama KP, Hinnov LA (eds.) Rock magnetic cyclostratigraphy 10–34

Kunming Prospecting Design Institute of China Nonferrous Metals Industry (KPDI) (2012) Exploration report of Pulang copper deposit, Yunnan Diqing Nonferrous Metal Co. Ltd

Laakso K, Peter JM, Rivard B, White HP (2016) Short-wave infrared spectral and geochemical characteristics of hydrothermal alteration at the Archean Izok Lake Zn-Cu-Pb-Ag volcanogenic massive sulfide deposit, Nunavut, Canada: Application in exploration target vectoring. Econ Geol 111:1223–1239

Lang JR, Gregory MJ, Rebagliati M, Payne JG, Oliver JL, Roberts K (2013) Geology and magmatic-hydrothermal evolution of the giant Pebble porphyry copper-gold-molybdenum deposit, southwest Alaska. Econ Geol 108:437–462

Leng CB, Zhang XC, Hu RZ, Wang SX, Zhong H, Wang WQ, Bi XW (2012) Zircon U-Pb and molybdenite Re–Os geochronology and Sr–Nd–Pb–Hf isotopic constraints on the genesis of the Xuejiping porphyry copper deposit in Zhongdian, Northwest Yunnan, China. J Asian Earth Sci 60:31–48

Leng CB, Huang QY, Zhang XC, Wang SX, Zhong H, Hu RZ, Bi XW, Zhu JJ, Wang XS (2014) Petrogenesis of the late Triassic volcanic rocks in the southern Yidun arc, SW China: Constraints from the geochronology, geochemistry, and Sr–Nd–Pb–Hf isotopes. Lithos 190–191:363–382

Leng CB, Cooke DR, Hou ZQ, Evans NJ, Zhang XC, Chen WT, Danišík M, McInnes BIA, Yang JH (2018) Quantifying exhumation at the giant Pulang porphyry Cu-Au deposit using U-Pb-He dating. Econ Geol 113:1077–1092

Leng CB, Gao JF, Chen WT, Zhang XC, Tian ZD, Guo JH (2018) Platinum-group elements, zircon Hf-O isotopes, and mineralogical constraints on magmatic evolution of the Pulang porphyry Cu-Au system, SW China. Gondwana Res 62:163–177

Li WC, Zeng PS, Hou ZQ, White NC (2011) The Pulang porphyry copper deposit and associated felsic intrusions in Yunnan Province, southwest China. Econ Geol 106:79–92

Li WK, Yang ZM, Cao K, Lu YJ, Sun MY (2019) Redox-controlled generation of the giant porphyry Cu–Au deposit at Pulang, southwest China. Contrib Mineral Petrol 174:12

Lian CY, Zhang G, Yuan CH (2005) Application of SWIR reflectance spectroscopy to Pulang porphyry copper ore district,Yunnan Province. Miner Depos 24: 621–637 (in Chinese with English abs.)

Liang HY, Sun WD, Su WC, Zartman RE (2009) Porphyry copper-gold mineralization at Yulong, China, promoted by decreasing redox potential during magnetite alteration. Econ Geol 104:587–596

Lowell JD, Guilbert JM (1970) Lateral and vertical alteration-mineralization zoning in porphyry ore deposits. Econ Geol 65:373–408

Lypaczewski P, Rivard B (2018) Estimating the $Mg^{\#}$ and Al^{VI} content of biotite and chlorite from shortwave infrared reflectance spectroscopy: Predictive equations and recommendations for their use. Int J Appl Earth Obs Geoinf 68:116–126

Neal LC, Wilkinson JJ, Mason PJ, Chang Z (2018) Spectral characteristics of propylitic alteration minerals as a vectoring tool for porphyry copper deposits. J Geochem Explor 184:179–198

Purucker ME, Clark DA (2011) Mapping and interpretation of the lithospheric magnetic field. In: Mandea M, Korte M (eds) Geomagnetic observations and models: Dordrecht. Springer, Netherlands, pp 311–337

Reed M (1997) Hydrothermal alteration and its relationships to ore fluid composition, In: Barnes KL (ed.) Geochemistry of hydrothermal ore deposits, Wiley: 303–366

Reid AJ, Wilson CJL, Liu S (2005) Structural evidence for the Permo-Triassic tectonic evolution of the Yidun Arc, eastern Tibetan Plateau. J Struct Geol 27:119–137

Reid A, Wilson CJL, Shun L, Pearson N, Belousova E (2007) Mesozoic plutons of the Yidun Arc, SW China: U/Pb geochronology and Hf isotopic signature. Ore Geol Rev 31:88–106

Richards JP (2003) Tectono-magmatic precursors for porphyry Cu-(Mo-Au) deposit formation. Econ Geol 98:1515–1533

Riveros K, Veloso E, Campos E, Menzies A, Véliz W (2014) Magnetic properties related to hydrothermal alteration processes at the Escondida porphyry copper deposit, northern Chile. Miner Deposita 49:693–707

Rochette P, Jackson M, Aubourg C (1992) Rock magnetism and the interpretation of anisotropy of magnetic susceptibility. Rev Geophys 30:209–226

Ross PS, Bourke A, Schnitzler N, Conly A (2019) Exploration vectors from near infrared spectrometry near the McLeod volcanogenic massive sulfide deposit, Matagami district, Québec. Econ Geol 114:613–638

Rusk BG, Reed MH, Dilles JH, Klemm LM, Heinrich CA (2004) Compositions of magmatic hydrothermal fluids determined by LA-ICP-MS of fluid inclusions from the porphyry copper–molybdenum deposit at Butte, MT. Chem Geol 210:173–199

Seedorff E, Dilles JH, Proffett JM Jr, Einaudi MT, Zurcher L, Stavast WJA, Johnson DA, Barton MD, Hedenquist JW, Thompson JFH, Goldfarb RJ, Richards JP (2005) Porphyry deposits: Characteristics and origin of hypogene features. Econ Geol 100 Anniv Volume 100: 251–298

Shah AK, Bedrosian PA, Anderson ED, Kelley KD, Lang J (2013) Integrated geophysical imaging of a concealed mineral deposit: A case study of the world-class Pebble porphyry deposit in southwestern Alaska. Geophysics 78:B317–B328

Sillitoe RH (2010) Porphyry copper systems. Econ Geol 105:3–41

Tappert M, Rivard B, Giles D, Tappert R, Mauger A (2011) Automated drill core logging using visible and near-infrared reflectance spectroscopy: a case study from the Olympic Dam IOCG deposit, South Australia. Econ Geol 106:289–296

Tappert MC, Rivard B, Giles D, Tappert R, Mauger A (2013) The mineral chemistry, near-infrared, and mid-infrared reflectance spectroscopy of phengite from the Olympic Dam IOCG deposit, South Australia. Ore Geol Rev 53:26–38

Thompson AJB, Hauff PL, Robitaille AJ (1999) Alteration mapping in exploration: Application of short-wave infrared (SWIR) spectroscopy. SEG Newsletter 39:15–27

Thompson AJB, Scott K, Huntington J, Yang K, Bedell R, Crósta AP, Grunsky E (2009) Mapping mineralogy with reflectance spectroscopy: Examples from volcanogenic massive sulfide deposits. Rev Econ Geol 16:25–40

Tian ZD, Leng CB, Zhang XC (2020) Provenance and tectonic setting of the Neoproterozoic meta-sedimentary rocks in SE Tibetan Plateau: Implications for tectonic affinity of the Yidun terrane. Precambr Res 344:105736

Tian ZD, Leng CB, Zhang XC, Tian F, Lai CK (2022) Late Neoproterozoic-early Paleozoic tectonic evolution and paleogeographic reconstruction of the eastern Tibetan Plateau: A perspective from detrital zircon U-Pb-Hf isotopic evidence. Precambr Res 377:106738

Tian F, Leng CB, Zhang XC, Tian ZD, Zhang W, Guo JH (2019) Application of short-wave infrared spectroscopy in Gangjiang porphyry Cu-Mo deposit in Nimu ore field, Tibet. Earth Sci-J China Univ Geosci 44:2143–2154 (in Chinese with English abs.)

Wang R, Cudahy T, Laukamp C, Walshe JL, Bath A, Mei Y, Young C, Roache TJ, Jenkins A, Roberts M, Barker A, Laird J (2017) White mica as a hyperspectral tool in exploration for the Sunrise Dam and Kanowna Belle gold deposits, western Australia. Econ Geol 112:1153–1176

Wang L, Percival JB, Hedenquist JW, Hattori K, Qin K (2021) Alteration mineralogy of the Zhengguang epithermal Au-Zn Deposit, northeast China: Interpretation of shortwave infrared

analyses during mineral exploration and assessment. Econ Geol 116:389–406

Wang SX, Zhang XC, Leng CB, Qin CJ, Ma DY, Wang WQ (2008) Zircon SHRIMP U-Pb dating of the Pulang porphyry copper deposit, northwestern Yunnan, China: The ore-forming time limitation and geological significance. Acta Petrologica Sinica 24: 2313–2321 (in Chinese with English abs.)

Yang K, Huntington JF, Browne PRL, Ma C (2000) An infrared spectral reflectance study of hydrothermal alteration minerals from the TeMihi sector of the Wairakei geothermal system. New Zealand Geothermics 29:377392

Yang K, Browne PRL, Huntington JF, Walshe JL (2001) Characterising the hydrothermal alteration of the broadlands-ohaaki geothermal system, New Zealand, using short-wave infrared spectroscopy. J Volcanol Geoth Res 106:53–65

Yang K, Lian C, Huntington JF, Peng Q, Wang Q (2005) Infrared spectral reflectance characterization of the hydrothermal alteration at the Tuwu Cu–Au deposit, Xinjiang, China. Miner Deposita 40:324–336

Yang K, Huntington J, Gemmell B, Scott KM (2011) Variations in composition and abundance of white mica in the hydrothermal alteration system at Hellyer, Tasmania, as revealed by infrared reflectance spectroscopy. J Geochem Explor 108:143–156

Yang ZM, Hou ZQ, Yang ZS, Qu HC, Li ZQ, Liu YF (2012) Application of short wavelength infrared (SWIR) technique in exploration of poorly eroded porphyry Cu district: A case study of Niancun ore district. Tibet Mineral Deposits 31:699–717

Yin A, Harrison TM (2000) Geologic evolution of the Himalayan-Tibetan orogen. Annu Rev Earth Planet Sci 28:211–280

Zeng PS, Li WC, Wang HP, Li H (2006) The Indosinian Pulang superlarge porphyry copper deposit in Yunnan, China: Petrology and chronology. Acta Petrologica Sinica 22: 989–1000 (in Chinese with English abs.)

Zhao ZF, Zhou JX, Lu YX, Chen Q, Cao XM, He XH, Fu XH, Zeng SH, Feng WJ (2021) Mapping alteration minerals in the Pulang porphyry copper ore district, SW China, using ASTER and WorldView-3 data: Implications for exploration targeting. Ore Geol Rev 134:104171